Supplement of Atmos. Chem. Phys., 26, 13387–13400, 2026
https://doi.org/10.5194/acp-26-13387-2026-supplement

Atmospheric Chemistry and Physics
Open Access
EGU

Supplement of

Complexation strength between organic carbon and transition metal ions dominates the photochemical conversion of SO_2 to sulfates

Shaojie Yang et al.

Correspondence to: Chong Han (hanch@smm.neu.edu.cn)

S1. Experimental section

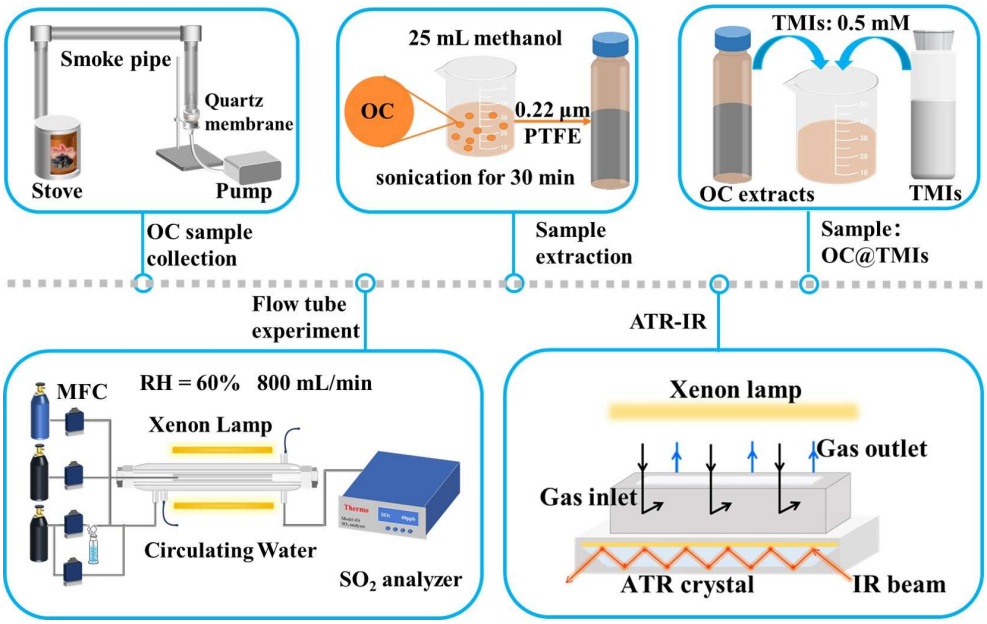

Figure S1. Diagram of OC samples preparation, flow tube reactor and in-situ attenuated total internal reflection infrared (ATR-IR) reaction cell.

S1.1. OC collection and preparation

The stove was commonly used in northern Chinese households and was acquired from the local market for the experiments. To address the ignition challenges of raw coal, solid alcohol and smokeless charcoal were initially employed to ignite approximately one-third of the coal sample (about 500 g). After successful ignition, the charcoal was removed and the remaining coal (around 1000 g) was added to sustain the combustion and generate smoke aerosols. The aerosols containing OC were collected onto quartz fiber filters (Whatman, Ø = 90 mm) positioned at the outlet of the flue. OC sampling artifacts were not quantified or corrected in this study. The organic carbon contents in the three independent sampling trials were measured to be 815.8 ± 53.2 μgC mL^{-1} using a total organic carbon analyzer (TOC-5000 RD, Metash). The typical instrumental detection limit was 0.05 μgC mL^{-1}. This suggests a good reproducibility among the sampling trials. Thus, possible sampling artifacts were expected to be similar among samples. All quartz fiber filters were pre-baked at 450 °C for 6 h to remove the carbon pollutants. After sample collection, the filters were sealed in aluminum foil and preserved at −20 °C until OC extraction. A custom-designed hole punch (6 mm diameter) was used to cut circular sections from the filter. OC was extracted by ultrasonication in methanol

(25 mL, ≥ 99.7%) for 30 min, as shown in Fig. S1. The obtained extracts passed through a 0.22 μm polytetrafluoroethylene (PTFE) membrane filter, and then they were stored under refrigeration (2 ℃) for subsequent analysis and experimental use.

S1.2. ICP-MS measurements

A 5 mL aliquot of the extracted OC solution was transferred to an amber glass vial and dried under a N_2 flow of 200 mL min^{-1}. Subsequently, 10 mL of ultrapure water was added and ultrasonicated for 30 min. The resulting solution was filtered through a 0.22 μm PTFE membrane. The background concentrations of Fe, Mn and Cu in OC were analyzed using the inductively coupled plasma-mass spectrometry (ICP-MS, 7800, Agilent Technologies Inc). Multi-element standard solutions were used for the calibration, and all calibration curves showed correlation coefficients higher than 0.999. The typical instrumental detection limits were 0.4 μg L^{-1} for Fe, 0.03 μg L^{-1} for Mn and 0.02 μg L^{-1} for Cu.

S1.3. Chemicals

Sodium chloride (NaCl), Iron(III) chloride hexahydrate ($FeCl_3 \cdot 6H_2O$, ≥ 99.9% metals basis), copper(II) chloride dihydrate ($CuCl_2 \cdot 2H_2O$, 99.99% metals basis), manganese(II) chloride tetrahydrate ($MnCl_2 \cdot 4H_2O$, 99.99% metals basis), zinc(II) chloride ($ZnCl_2$, 99.95% metals basis), chromium(III) chloride hexahydrate ($CrCl_3 \cdot 6H_2O$, ≥ 99.9% metals basis), cobalt(II) chloride hexahydrate ($CoCl_2 \cdot 6H_2O$, ≥ 99.9% metals basis), magnesium(II) chloride hexahydrate ($MgCl_2 \cdot 6H_2O$, ≥ 99.9% metals basis), calcium(II) chloride anhydrous ($CaCl_2$, ≥ 99.9% metals basis), nickel(II) chloride hexahydrate ($NiCl_2 \cdot 6H_2O$, ≥ 99.9% metals basis) and aluminum(III) chloride ($AlCl_3$, 99.99% metals basis) were purchased from Aladdin.

S1.4. Flow tube experiments

The reactor temperature was maintained at 298 ± 2 K by circulating water through the outer jacket. A relative humidity (RH) of 60% was obtained by regulating the ratio of humidified N_2 in the gas flow, and RH was recorded via a hygrometer (Center 314). Solar irradiation was simulated by two 250 W xenon lamps, and the corresponding spectral irradiance is presented in Fig. S2. The total irradiance in the wavelength range of 300−700 nm was determined to be 1.05×10^{16} photons cm^{-2} s^{-1} with a spectroradiometer (ULS2048CL-EVO, Avantes). SO_2 was fed into the reactor via a movable injector, and a synthetic air flow (N_2/O_2, 800 mL min^{-1}, SO_2 of 40 ppb) was supplied to ensure laminar flow conditions. SO_2 concentration of 40 ppb was chosen, and it represented atmospherically relevant SO_2 level (Liu et al., 2022). Control experiments confirmed that SO_2 loss was negligible under both dark and irradiation conditions in the blank reactor (Fig. S3).

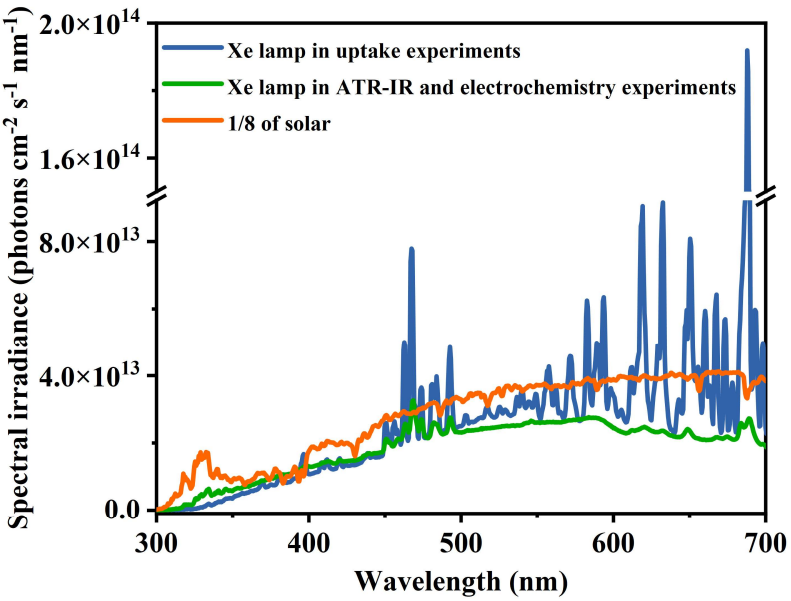

Figure S2. The spectral irradiance of xenon lamps and the solar spectrum measured for the 48° solar zenith clear sky at Shenyang (41.45 N, 123.25 E) on May 21st, 2024, at local time 12:00.

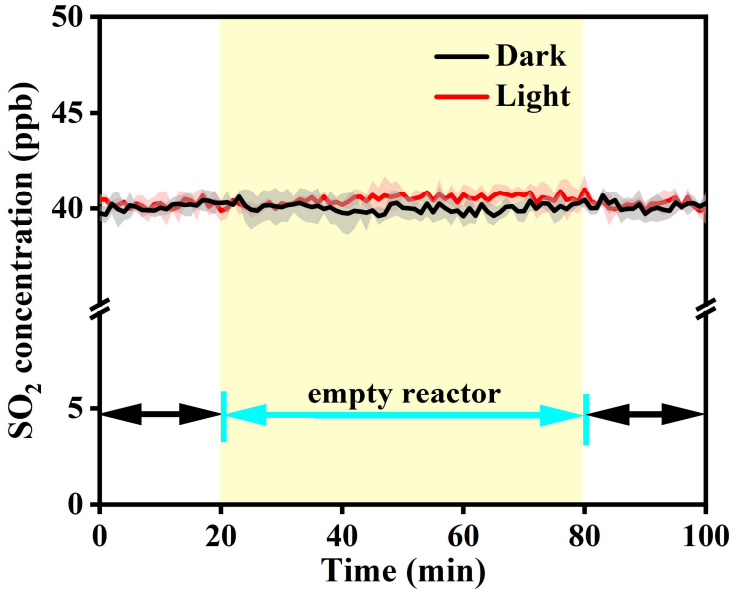

Figure S3. The uptake of SO_2 on empty reactor sample in the dark and under irradiation (1.05 × 10^{16} photons cm^{-2} s^{-1}). All experiments were performed at 40 ppb SO_2, 298 K and 60% RH.

S1.5. Calculation of SO_2 uptake coefficient

The geometric uptake coefficients (γ) of SO_2 were calculated through the Eq. (S1),

$$\frac{\ln (C_0/C_t)}{t} = k_{obs} = \frac{\gamma v}{2r_{tube}} \quad \text{(S1)}$$

where C_0 represents the initial SO_2 concentration (ppb); C_t means the SO_2 concentration (ppb) at a certain exposure time; t corresponds to the residence time (s) of SO_2 in the reactor. The observed first-order rate constant is expressed as k_{obs} (s^{-1}). The average molecular velocity (v) of SO_2 is 314 m s^{-1}, and the radius of the sample tube (r_{tube}) is 0.5 cm. The initial uptake coefficients (γ_i) were obtained from the maximum SO_2 uptake on OC within the first 1−2 min of the reaction, while the steady-state uptake coefficients (γ_{ss}) were derived from stable SO_2 concentrations between 60 and 80 min.

S1.6. Attenuated total reflection infrared spectroscopy

Samples (600 μL) were coated onto ZnSe plates and dried in an N_2 stream (100 mL min^{-1}) at room temperature. The samples were then purged with synthetic air (200 mL min^{-1}, N_2/O_2) at 298 K and 60% RH in the dark until the infrared spectrum stabilized. When samples were exposed to 2 ppm SO_2, the IR spectra were collected in the range of 4000−650 cm^{-1} at 4 cm^{-1} resolution for 100 scans, and the fresh samples served as the background. A SO_2 concentration of 2 ppm was used in the situ attenuated total reflection infrared (ATR-IR) experiments to improve spectral signals. A 500 W xenon lamp was used as the light source, with its irradiance shown in Fig. S2. Blank ZnSe control experiments were conducted, and the weak IR signals indicated that the reaction of SO_2 with ZnSe plate was negligible (Yang et al., 2025).

S1.7. Ion chromatography

To ensure that sulfates formed in the experiments were above the ion chromatography (IC) detection limit, the SO_2 concentration in the flow tube reactor was set at 200 ppb. Surface sulfates were extracted with 25 mL of 5% formaldehyde aqueous solution, and gaseous H_2SO_4 was captured in a glass tube containing 10 mL 5% formaldehyde solution at the reactor outlet. Formaldehyde aqueous solution can inhibit the oxidation of sulfites (Li et al., 2021). All solutions were filtered through 0.22 μm PTFE membranes. During the IC analysis, a 13 mM KOH eluent was employed at 35 ℃ with a flow rate of 1 mL min^{-1}. Sulfate calibration curves were established using standard sulfate solutions, and the correlation coefficient was 0.999. The detection and quantification limits for sulfate were 0.0005 and 0.001 mg L^{-1}, respectively. The lowest sulfate concentration reported in this study was 0.00579 mg L^{-1}, which was above the quantification limit. The background sulfate concentration in the fresh OC samples was 0.0620 ± 0.0058 mg L^{-1}. This has been subtracted from the sulfate concentrations measured after the reaction.

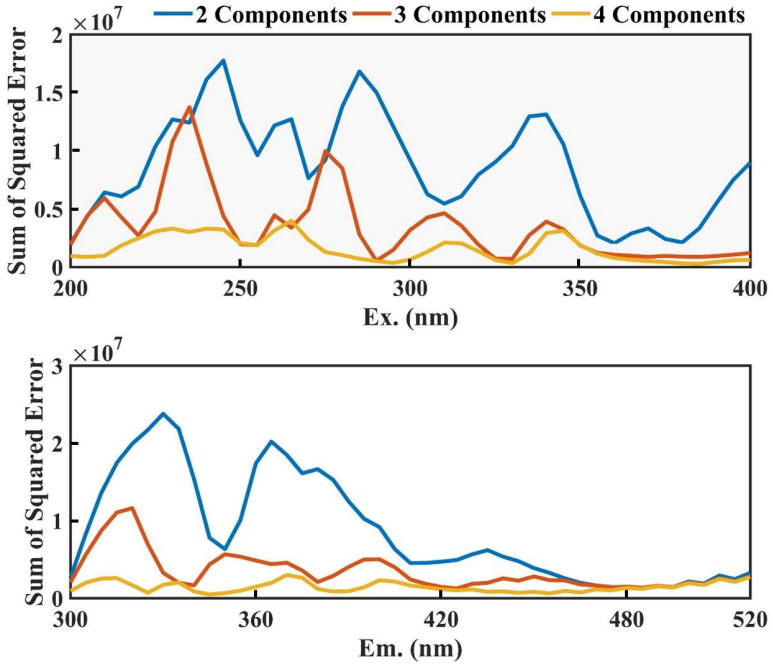

Figure S4. Sum of squared error plots showing the error as a function of Ex. and Em. wavelengths for varying component numbers in the spectral decomposition. The top panel presents the error for different numbers of components (2, 3 and 4 components) as a function of excitation wavelength (200−400 nm), while the bottom panel shows the error as a function of emission wavelength (300−520 nm). The blue, red, and yellow curves represent the sum of squared error for 2, 3 and 4 components, respectively.

S1.8. Electrochemical testing procedures

The three-electrode system comprised an Ag/AgCl reference electrode, a platinum counter electrode and a glassy carbon working electrode. 2, 2'-azino-bis (3-ethylbenzothiazoline-6-sulfonic acid) (ABTS) was selected as the reaction mediator for electron donating capacities (EDC). Initially, 35 mL phosphate buffer solution was added to the reaction cell and purged with nitrogen (N_2) for 10 minutes to eliminate atmospheric interference. The electrochemical workstation was operated in “Amperometric i-t curve parameters” mode at a redox potential (Eh) of +0.41 V. The xenon lamp was used to simulate solar irradiation, and its irradiance was shown in Fig. S2. Once the system stabilized, 0.5 mM ABTS solution was introduced as the redox mediator, followed by the addition of samples at 20-minute intervals in volumes of 0.1, 0.2, 0.3 and 0.4 mL, respectively.

S1.9. H_2O_2 testing procedure

After 1 h of irradiation, the reaction products deposited on the inner wall of the flow-tube reactor were rapidly extracted with 9 mL of methanol. 3 mL of the extract was subsequently mixed with 3 mL of a 5% *v*/*v* $TiOSO_4$ solution. The mixture was incubated in the dark for 15 min, and then the absorbance at 405 nm was recorded using a UV-vis spectrophotometer. To correct potential interference from the samples, the background test was conducted using parallel samples without the titanium reagent.

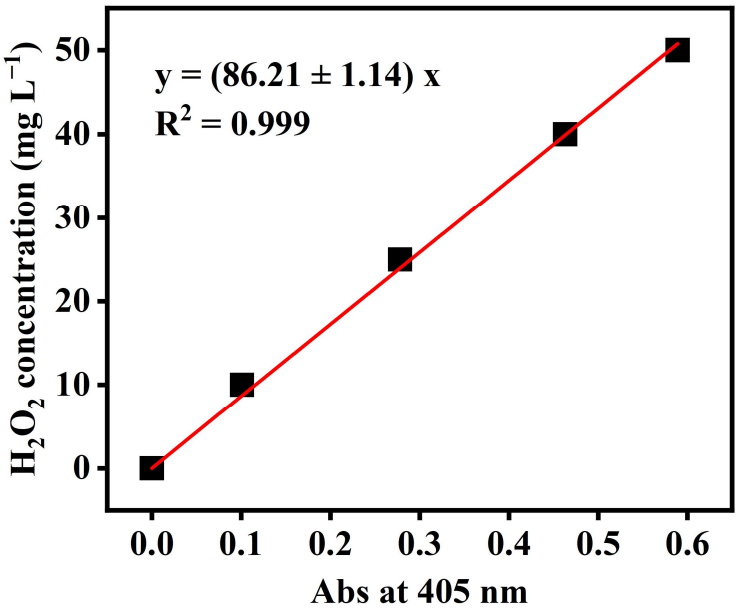

Figure S5. The standard curve of H_2O_2 obtained by using $TiOSO_4$ as an indicator.

S1.10. Energy calculations

The complexation energy ($E_{complex}$) between ligands and transition metal ions was calculated according to Eq. (S2),

$$E_{complex} = E_{total\ complex} - (E_L + E_M) \quad (S2)$$

where $E_{total\ complex}$ is the total energy (kJ mol^{-1}) of the optimized metal−ligand complex; E_L and E_M are the energy (kJ mol^{-1}) of the isolated ligand and transition metal ions, respectively. A more negative $E_{complex}$ indicates stronger complexation between the ligand model and TMIs.

The adsorption energy (E_{ad}) for O_2 on the surfaces of the samples could be estimated by Eq. (S3),

$$E_{ad} = E_{AB} - (E_A + E_B) \quad (S3)$$

where E_{AB}, E_A and E_B refer to the single point energy (kJ mol^{-1}) of the optimized complex with adsorbed O_2, the corresponding model surface without O_2 and isolated O_2, respectively. A more negative E_{ad} indicates stronger O_2 adsorption.

S2. SO_2 uptake and sulfate formation

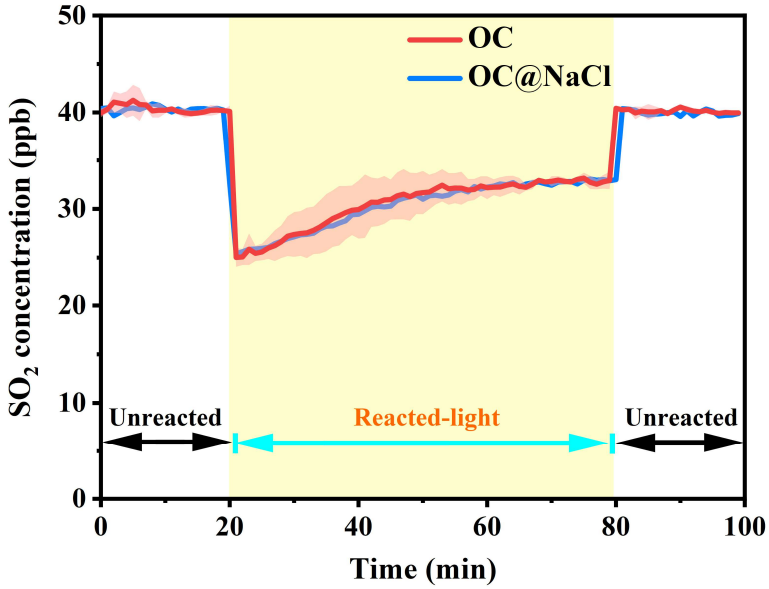

Figure S6. Temporal variation in the SO_2 concentration on OC (red line) and OC@NaCl (blue line) under irradiation. Reaction conditions: irradiance of 1.05×10^{16} photons cm^{-2} s^{-1}, 40 ppb SO_2, 298 K and 60% RH.

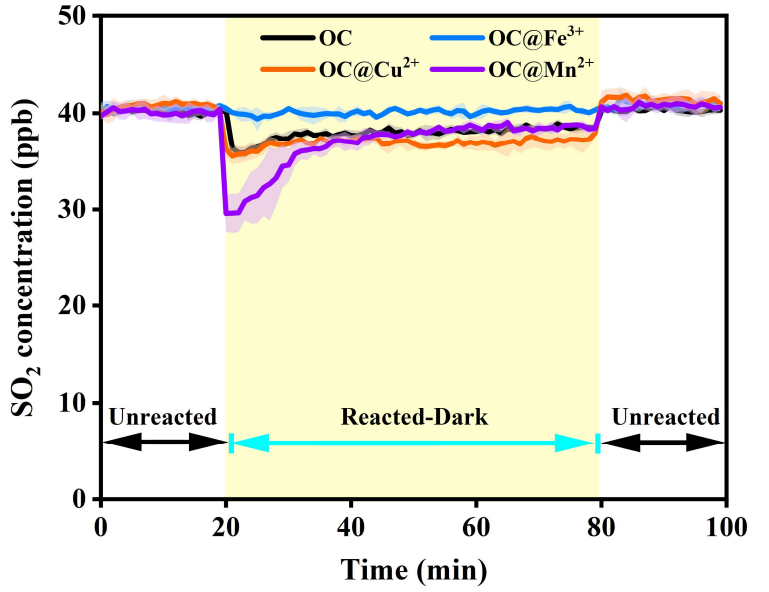

Figure S7. Temporal variations of the SO_2 concentration during the heterogeneous reaction of SO_2 with OC, OC@Fe^{3+}, OC@Cu^{2+} and OC@Mn^{2+} in the dark. Reaction conditions: 40 ppb SO_2, 298 K and 60% RH.

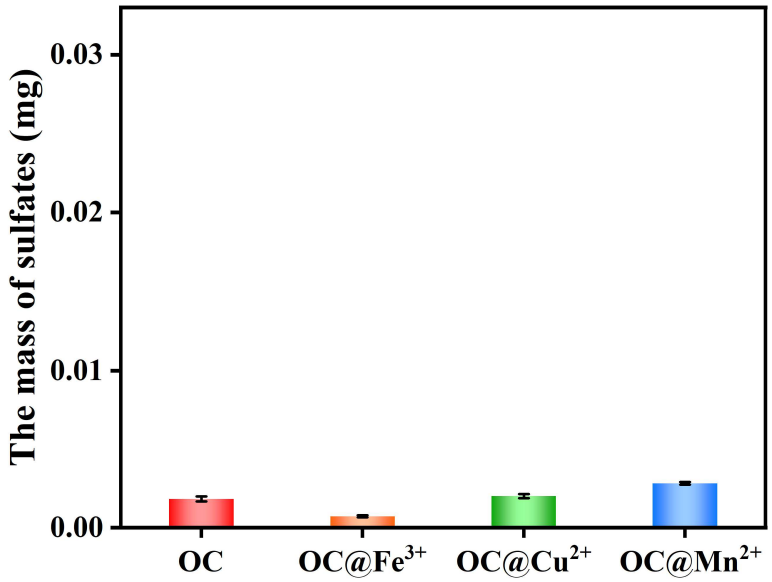

Figure S8. Mass of sulfates produced on OC and OC@TMIs after the 10 h reaction with SO_2 in the dark. Reaction conditions: 200 ppb SO_2, 298 K and 60% RH.

S3. Complexation evidence of OC with metal ions

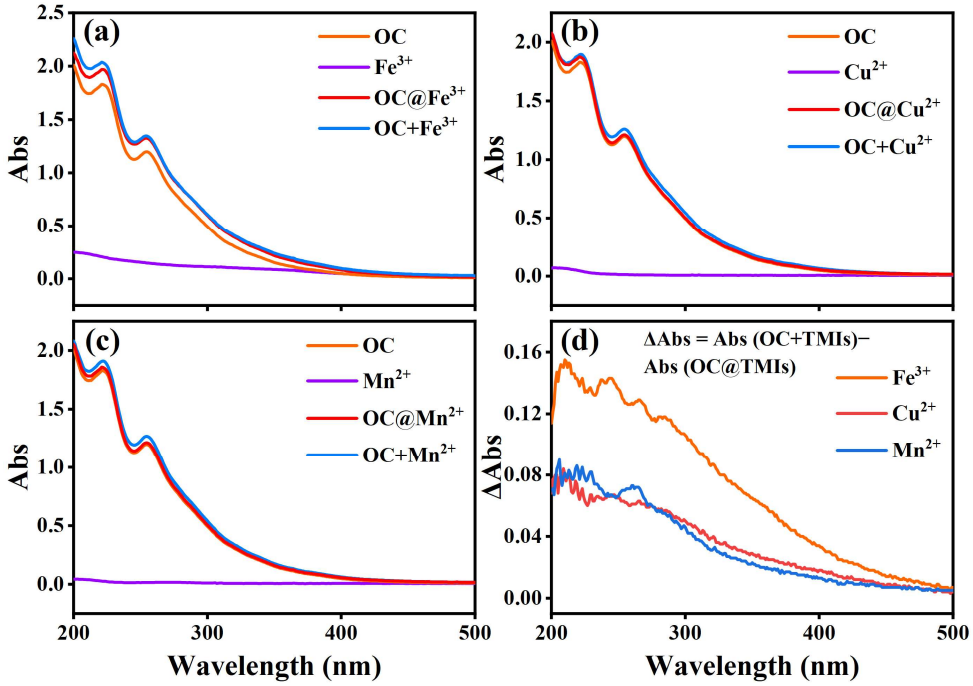

Figure S9. (a–c) The UV-vis spectra of OC, $FeCl_3$, OC@Fe^{3+}, OC+Fe^{3+}, $CuCl_2$, OC@Cu^{2+}, OC+Cu^{2+}, $MnCl_2$, OC@Mn^{2+} and OC+Mn^{2+} (For OC+TMIs, the absorbance was the arithmetic sum of that measured for OC and TMIs in separate experiments). (d) Differential absorbance spectra (ΔAbs) by subtracting the absorbance of OC@TMIs from that of OC+TMIs (Fe^{3+}, Cu^{2+} and Mn^{2+}).

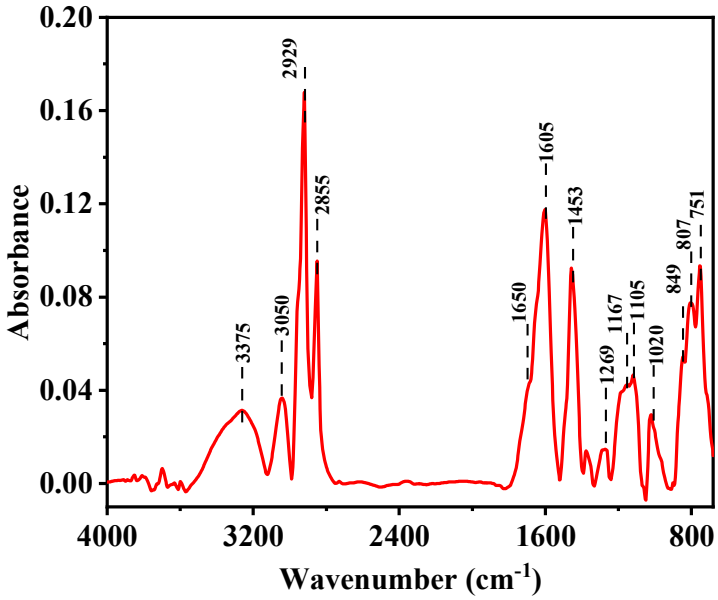

Figure S10. FT-IR spectra of OC.

Table S1. Assignments of functional groups in the FT-IR spectra of OC.

Wavenumber (cm^{-1})	Functional Groups
3375	Stretching vibration of O−H of carboxyl, phenol and alcohol (Hay and Myneni, 2007)
3050	Stretching vibration of aromatic C−H (Sun et al., 2019)
2929	Asymmetric stretching vibration of C−H (Chen et al., 2016)
2855	Symmetric stretching vibration of C−H (Chen et al., 2016)
1650, 1605	Stretching vibration of aromatic C=O (Han et al., 2012)
1453	Asymmetric stretching vibration of methyl C−H (Sun et al., 2019)
1269, 1167	Stretching vibration of phenolic C−OH (Sun et al., 2019)
1105, 1020	Stretching vibration of C−O in ethers (Sun et al., 2019)
849, 807, 751	Out-of-plane bending vibration of aromatic C−H (Gaffney et al., 2015)

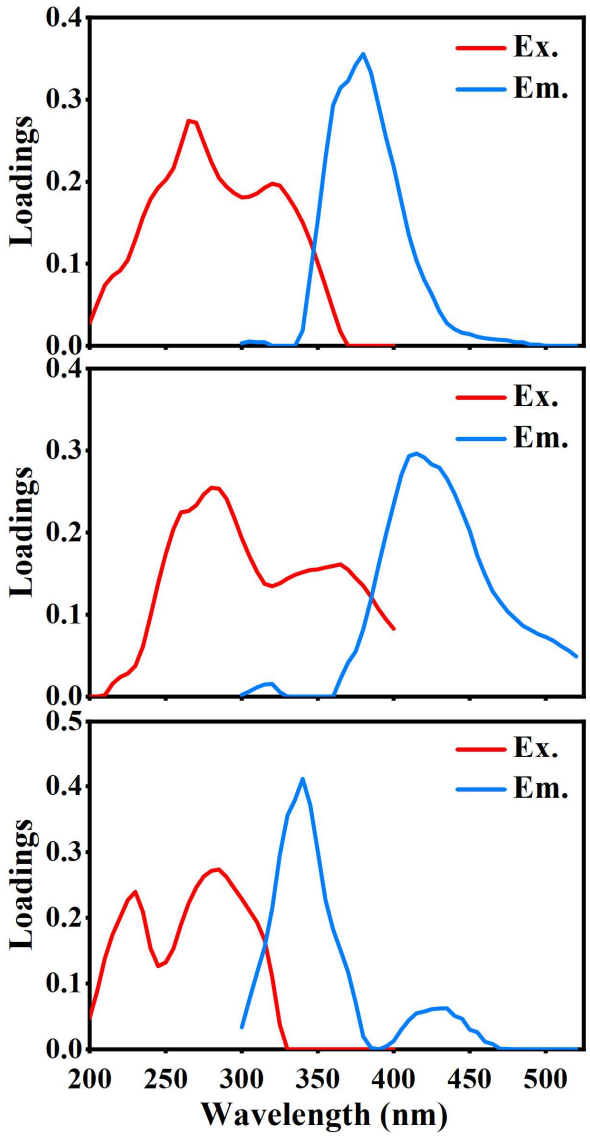

Figure S11. Three components extracted by the parallel factor analysis (PARAFAC).

Table S2. Peak position and possible components of different chromophores (C1−C3).

Composition	Ex. (nm)	Em. (nm)	Possible components
C1	265/320	380	Lowly oxidized OC
C2	285/370	420	Highly oxidized OC (oxygen-containing polar functional groups such as hydroxyl and carboxyl groups)
C3	200/260	340	Protein-like chromophores

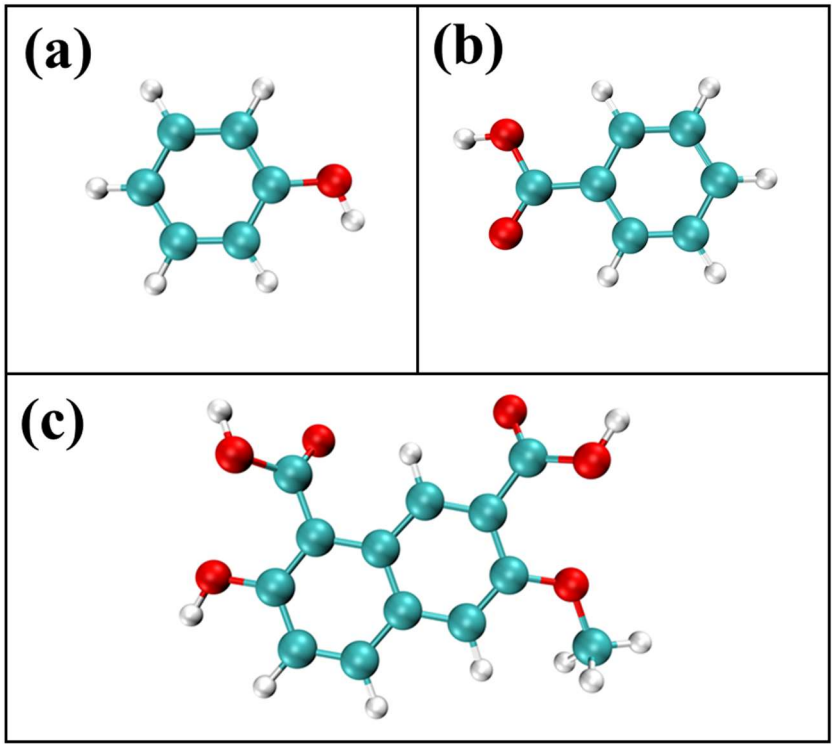

Figure S12. Configuration diagram of organic species: (a) phenol (PH), (b) benzoic acid (BA) and (c) model substance (MS). Oxygen atoms, carbon atoms and hydrogen atoms are shown in red, cyan and light gray, respectively.

S3.1. Complexation model construction

To better simulate real conditions in weakly acidic or aerosol environments, all ligands were modeled in their neutral forms. The initial coordination model was constructed by positioning the molecules near the transition metal center, with donor atoms oriented toward the metal at an initial distance of ~2.0 Å. PH contained a hydroxyl (−OH) group, and its oxygen donated a lone pair for monodentate coordination. The carboxyl group (−COOH) within BA provided a carbonyl (C=O) and a hydroxyl (C−O) oxygen, enabling bidentate coordination and enhancing complex stability. In MS molecule, −OH and −COOH groups were placed adjacently, allowing for the formation of six-membered chelate rings upon metal binding. This chelation strengthened the coordination interaction but also improved environmental representativeness. Carbonyl oxygen (C=O) preferentially acted as the coordination site due to its higher electron density and favorable spatial orientation.

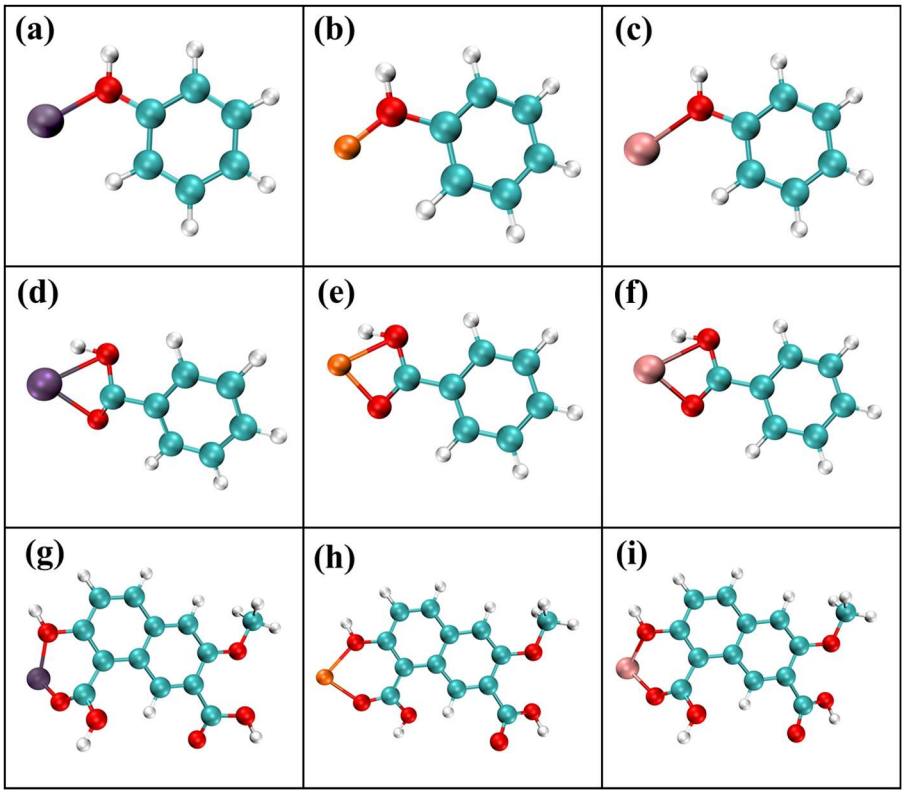

Figure S13. Configuration diagram of complexation model: (a−c) PH complexes, (d−f) BA complexes and (g−i) MS complexes. Oxygen atoms, carbon atoms, hydrogen atoms, iron atoms, copper atoms and manganese atom are shown in red, cyan, light gray, purple, orange and pink, respectively.

Table S3. Complexation energies of TMIs with BA, PH and MS.

Samples	Complexation energy (kJ mol^{-1})
PH@Fe^{3+}	−435.53
PH@Cu^{2+}	−102.42
PH@Mn^{2+}	−4.31
BA@Fe^{3+}	−505.01
BA@Cu^{2+}	−368.97
BA@Mn^{2+}	−295.53
MS@Fe^{3+}	−531.76
MS@Cu^{2+}	−107.29
MS@Mn^{2+}	−41.25

S4. Mechanism verification

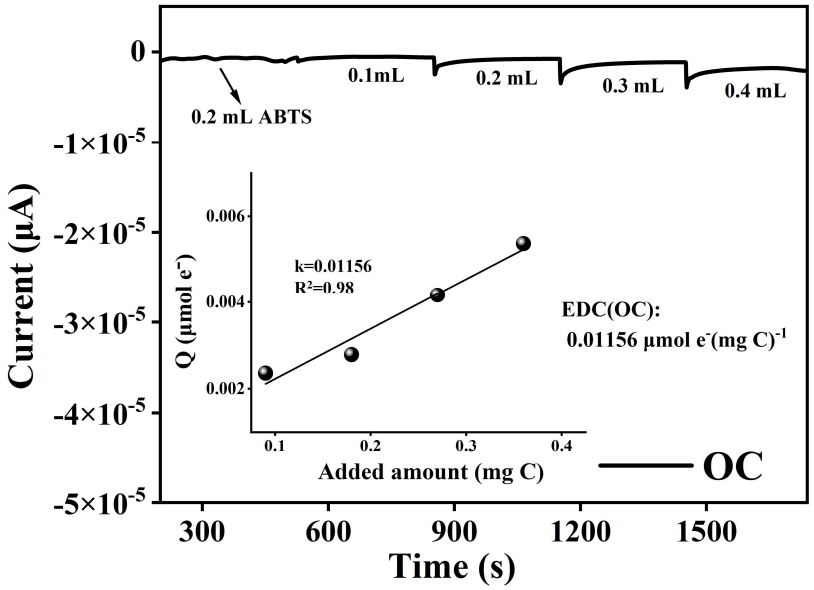

Figure S14. The oxidation current response in mediated electrochemical oxidation (MEO) and EDC of OC.

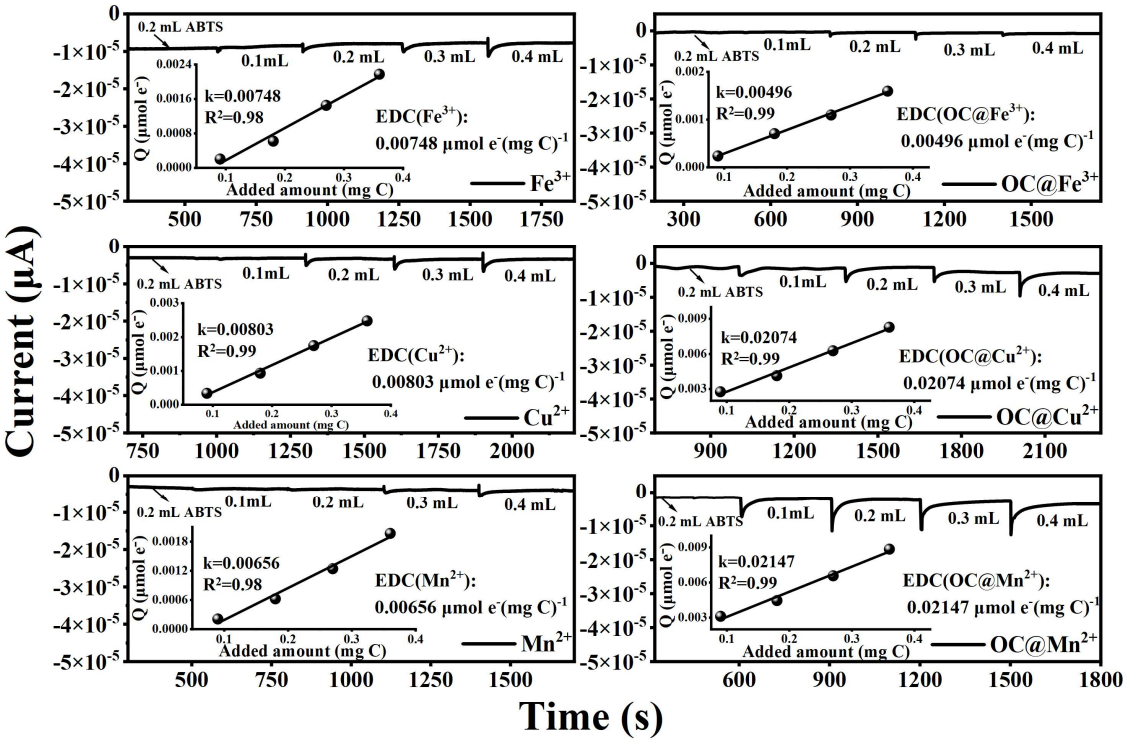

Figure S15. The oxidation current response in MEO and EDC of Fe^{3+}, OC@Fe^{3+}, Cu^{2+}, OC@Cu^{2+}, Mn^{2+} and OC@Mn^{2+}.

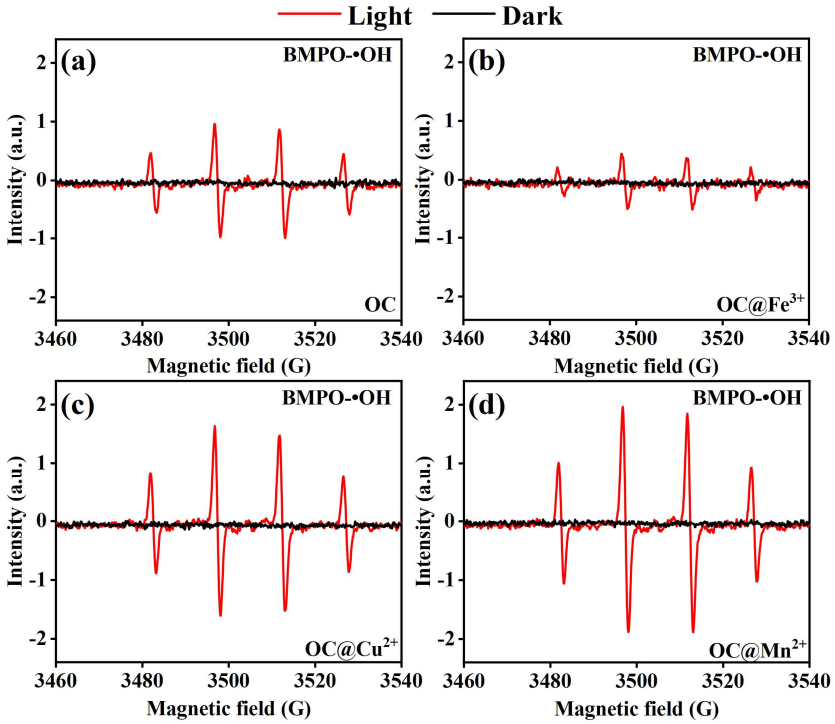

Figure S16. EPR spectra of BMPO-•OH adducts for (a) OC, (b) OC@Fe^{3+}, (c) OC@Cu^{2+} and (d) OC@Mn^{2+} in the dark and under irradiation.

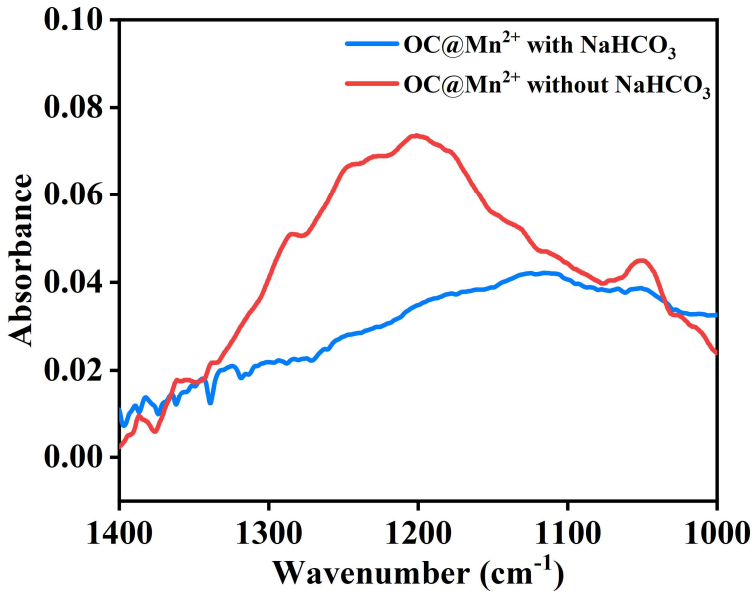

Figure S17. Sulfate formation on OC@Mn^{2+} with and without $NaHCO_3$ in the range of 1400−1000 cm^{-1} under irradiation (7.40×10^{15} photons cm^{-2} s^{-1}). All experiments were performed at 2 ppm SO_2, 298 K and 60% RH.

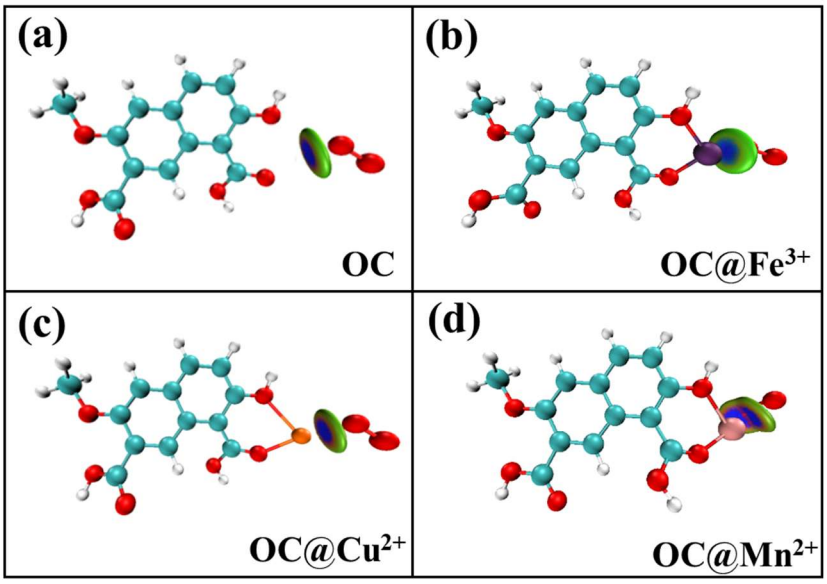

Figure S18. The IGMH diagram of the adsorption of O_2 on (a) MS, (b) MS@Fe^{3+}, (c) MS@Cu^{2+} and (d) MS@Mn^{2+}. The O_2 adsorption structure was established by placing the O_2 molecule approximately 2.0 Å from the metal center, with its molecular axis aligned toward the coordination site.

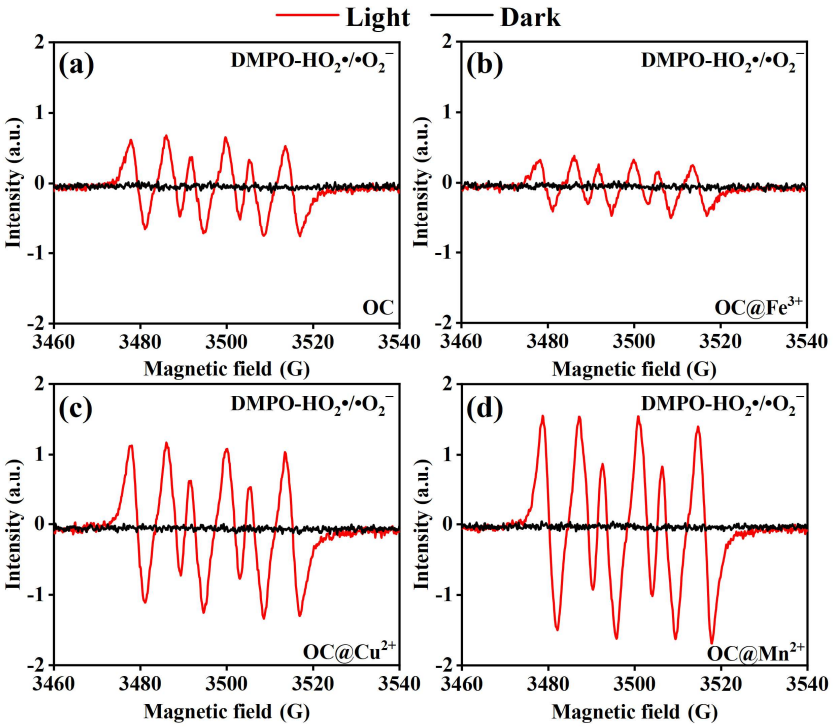

Figure S19. EPR spectra of DMPO-HO_2•/•O_2^- adducts for (a) OC, (b) OC@Fe^{3+}, (c) OC@Cu^{2+} and (d) OC@Mn^{2+} in the dark and under irradiation.

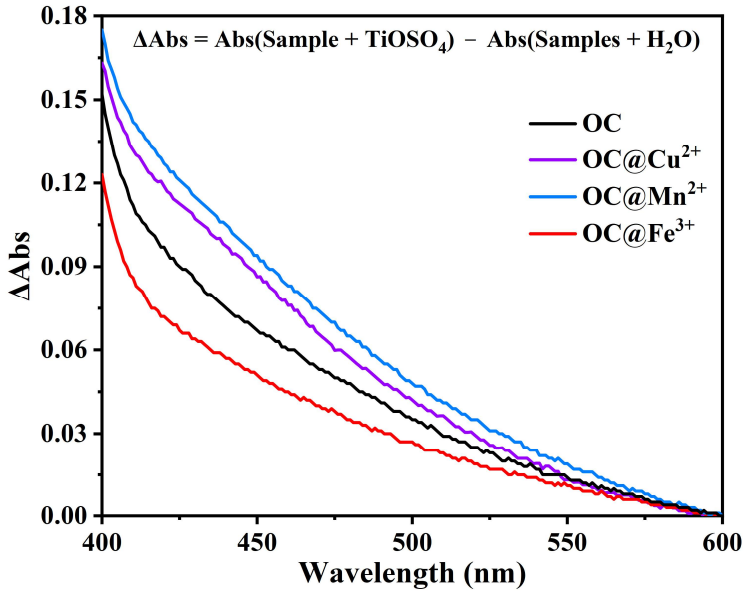

Figure S20. Differential absorbance spectra (ΔAbs) by subtracting the absorbance of samples+H_2O from that of samples+$TiOSO_4$ (OC, OC@Cu^{2+}, OC@Mn^{2+} and OC@Fe^{3+}).

S5. Discussion

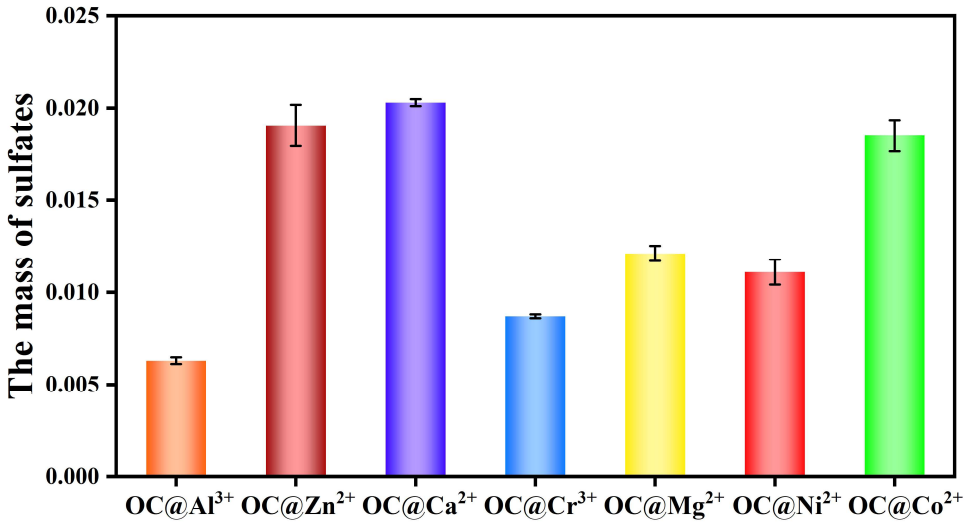

Figure S21. Mass of sulfates produced on OC@TMIs after the 10 h reaction with SO_2 under irradiation. Reaction conditions: irradiance of 1.05×10^{16} photons cm^{-2} s^{-1}, 200 ppb SO_2, 298 K and 60% RH.

References

Chen, Q., Ikemori, F., Higo, H., Asakawa, D., and Mochida, M.: Chemical structural characteristics of HULIS and other fractionated organic matter in urban aerosols: Results from mass spectral and FT-IR analysis, Environ. Sci. Technol., 50, 1721−1730, https://doi.org/10.1021/acs.est.5b05277, 2016.

Gaffney, J. S., Marley, N. A., and Smith, K. J.: Characterization of fine mode atmospheric aerosols by raman microscopy and diffuse reflectance FTIR, J. Phys. Chem. A, 119, 4524−4532, https://doi.org/10.1021/jp510361s, 2015.

Han, C., Liu, Y., Ma, J., and He, H.: Key role of organic carbon in the sunlight-enhanced atmospheric aging of soot by O_2, Proc. Natl. Acad. Sci. USA, 109, 21250−21255, https://doi.org/10.1073/pnas.1212690110, 2012.

Hay, M. B. and Myneni, S. C. B.: Structural environments of carboxyl groups in natural organic molecules from terrestrial systems. Part 1: Infrared spectroscopy, Geochim. Cosmochim. Acta, 71, 3518−3532, https://doi.org/10.1016/j.gca.2007.03.038, 2007.

Li, K., Fang, X., Wang, T., Gong, K., Ali Tahir, M., Wang, W., Han, J., Cheng, H., Xu, G., and Zhang, L.: Atmospheric organic complexation enhanced sulfate formation and iron dissolution on nano α-Fe_2O_3, Environ. Sci.: Nano, 8, 698−710, https://doi.org/10.1039/d0en01220c, 2021.

Liu, X., Ran, L., Lin, W., Xu, X., Ma, Z., Dong, F., He, D., Zhou, L., Shi, Q., and Wang, Y.: Measurement report: Variations in surface SO_2 and NO_x mixing ratios from 2004 to 2016 at a background site in the North China Plain, Atmos. Chem. Phys., 22, 7071−7085, https://doi.org/10.5194/acp-22-7071-2022, 2022.

Sun, J., Shen, Z., Zhang, Y., Zhang, Q., Wang, F., Wang, T., Chang, X., Lei, Y., Xu, H., Cao, J., Zhang, N., Liu, S., and Li, X.: Effects of biomass briquetting and carbonization on $PM_{2.5}$ emission from residential burning in Guanzhong Plain, China, Fuel, 244, 379−387, https://doi.org/10.1016/j.fuel.2019.02.031, 2019.

Yang, H., Yang, W., Nan, X., Tang, N., and Han, C.: Significantly surfactant-enhanced photochemical conversion of SO_2 to sulfates on photosensitive substances, J. Environ. Sci., 156, 539−548, https://doi.org/10.1016/j.jes.2024.10.014, 2025.